1 ## 2. Supplementary Information:

2 ### A. Flat Files

3

Item	Present?	Filename This should be the name the file is saved as when it is uploaded to our system, and should include the file extension. The extension must be .pdf	A brief, numerical description of file contents. i.e.: *Supplementary Figures 1-4, Supplementary Discussion, and Supplementary Tables 1-4.*
Supplementary Information	Yes	Gohl_SI_final.pdf	Supplementary Figures S1-12, Supplementary Table S1, and Supplementary Discussion
Reporting Summary	No		

4

5

6

7

8

9 # Engineering stable electrocatalysts by synergistic stabilization between
10 carbide cores and Pt shells

11

12 **Daniel Göhl[a,b,§], Aaron Garg[c,§], Paul Paciok[d], Karl J. J. Mayrhofer[a,e], Marc Heggen[d], Yang**
13 **Shao-Horn[f], Rafal E. Dunin-Borkowski[d], Yuriy Román-Leshkov[c,*], Marc Ledendecker[a,*]**

14 [a]Department of Interface Chemistry and Surface Engineering, Max-Planck-Institut für Eisenforschung, 40237
15 Düsseldorf, Germany
16 [b]Faculty of Chemistry and Biochemistry, Ruhr-Universität Bochum, 44780 Bochum, Germany
17 [c]Department of Chemical Engineering, Massachusetts Institute of Technology, Cambridge, MA 02139, USA
18 [d]Ernst Ruska-Centre for Microscopy and Spectroscopy with Electrons and Peter Grünberg Institute,
19 Forschungszentrum Jülich GmbH, 52425 Jülich, Germany
20 [e]Research Unit B Electrocatalysis, Helmholtz-Institut Erlangen-Nürnberg, 91058 Erlangen, Germany
21 [f]Department of Mechanical Engineering and Department of Materials Science and Engineering, Massachusetts
22 Institute of Technology, Cambridge, MA 02139, USA
23 *Corresponding authors: Marc Ledendecker, m.ledendecker@mpie.de; Yuriy Román-Leshkov, yroman@mit.edu
24 §These authors contributed equally to this work.

25 **Core-shell particles with earth-abundant cores represent an effective design**
26 **strategy for improving the performance of noble metal catalysts, while**
27 **simultaneously reducing the content of expensive noble metals.[1-4] However, the**

structural and catalytic stabilities of these materials often suffer during the harsh conditions encountered in important reactions, such as the oxygen reduction reaction (ORR).[3-5] Here, we demonstrate that atomically-thin Pt shells stabilize titanium tungsten carbide cores, even at highly oxidizing potentials. *In situ*, time-resolved experiments showed how the Pt coating protects the normally labile core against oxidation and dissolution, and detailed microscopy studies revealed the dynamics of partially and fully coated core-shell nanoparticles during potential cycling. Particles with complete Pt coverage precisely maintained their core-shell structure and atomic composition during accelerated electrochemical aging studies consisting of over 10,000 potential cycles. The exceptional durability of fully coated materials highlights the potential of core-shell architectures utilizing earth-abundant transition metal carbide (TMC) and nitride (TMN) cores for future catalytic applications.

The development of core-shell nanostructures with controllable size, shell thickness, surface facets, and composition vastly expands the possibility for engineering noble metal catalysts with enhanced performance.[4] Numerous core-shell systems have been synthesized for catalytic applications, very often with other noble metal cores, such as Ru,[6,7] Pd,[5,8] Ag,[9] and Ir[10] with marginal cost benefits. Critically, these core-shell materials along with those comprising earth-abundant, metallic cores (e.g., Fe, Co, and Ni) form intrinsically metastable structures with miscible core and shell elements that degenerate during electrochemical cycling or annealing due to metal leaching or migration.[5,7,8,11] These instabilities result in significant losses in active surface area and performance over time, imposing major barriers for the broad usage of core-shell architectures in industrial applications, where stability is essential. This is especially true for fuel cell technologies, the commercialization of which has been hindered by the poor durability of ORR catalysts.[3,12-14]

Early TMCs and TMNs are ideal core materials owing to their thermal and chemical stability, electrical conductivity, low cost, and intrinsic ability to bind strongly to noble metals while still being immiscible with them.[15,16] Unfortunately, the formation of surface oxides or carbon on TMCs and TMNs presents a difficult synthetic challenge for the deposition of atomically-thin, uniform noble metal shells.[15,17] As a result, only a few examples of core-shell systems comprising noble metal shells and TMC or TMN cores have been reported.[18,19] Recently, we demonstrated a versatile synthetic method that circumvents these challenges via a high temperature self-assembly allowing for the synthesis of Pt shells on titanium tungsten carbide (Pt/TiWC) and titanium tungsten nitride (Pt/TiWN) cores with controllable shell coverage.[15,20,21] These core-shell materials display unique catalytic properties resulting from bonding interactions between the shell and the core, including weakened adsorbate binding and extremely high sinter-resistance, but their durability in electrochemical environments has received only minor attention to date.

Here, we conducted a detailed examination of the electrochemical stability of Pt/TiWC and Pt/TiWN nanoparticles (NPs) as a function of two different Pt coverages to help identify possible underlying degradation mechanisms. Specifically, a scanning flow cell with inductively coupled plasma mass spectrometry (SFC-ICP-MS) was used to measure metal dissolution as a function of potential, and identical location scanning

73 transmission electron microscopy (IL-STEM) paired with energy dispersive X-ray
74 spectroscopy (EDX) was used to track changes to the structure of individual particles. In
75 addition to possessing exemplary structural stability, fully coated core-shell materials
76 demonstrated durability as ORR catalysts. Together, these results provide important
77 insights on the design of stable core-shell catalysts with earth-abundant elements.

78 To determine the effect of the Pt shell coverage on the electrochemical stability, we
79 synthesized nominal 0.7 monolayer (ML) Pt/TiWC and 2 ML Pt/TiWC using methods
80 previously reported by our group.[15,20] The carbon-supported materials (*ca.* 20 wt.%
81 core-shell particles, Ti:W ratio *ca.* 10:90) were characterized by transmission electron
82 microscopy (TEM) (Figure S1) to determine particle size distributions (PSDs) and ICP-
83 MS (Table S1) to determine elemental compositions. The PSDs for 0.7 ML Pt/TiWC and
84 2 ML Pt/TiWC were 5.1 ± 1.3 nm and 6.6 ± 1.8 nm, respectively. The average Pt shell
85 thickness was then estimated from the average particle size and the elemental
86 composition.

87 As a first indication of stability, the dissolution of carbide-based core-shell particle
88 elements was examined *in situ* via SFC-ICP-MS. To establish a clear relationship
89 between the applied potential and metal dissolution, a slow cyclic voltammetry (CV)
90 scan was conducted at 2 mV s^{-1} from 0.0 to 1.5 V$_{RHE}$ in 0.1 M HClO$_4$ on the core-shell
91 NPs as well as on bare TiWC NPs supported on carbon (Figure 1a).[22] For the Pt-
92 containing samples, oxidation of Pt occurs around 1.0 V$_{RHE}$ and is accompanied by
93 slight dissolution up to 1.5 V$_{RHE}$, but the majority of Pt dissolution occurs during the
94 cathodic scan when the formed Pt oxides are reduced to Pt^0 near 0.7 V$_{RHE}$, as
95 previously shown by Topalov et al.[23] For bare face centered cubic (fcc) TiWC NPs, the
96 CV scan showed oxidation beginning at *ca.* 0.6 V$_{RHE}$, coinciding directly with severe W
97 dissolution (Ti dissolution profile in Figure S2). Previous studies on bulk hexagonal WC
98 showed similar behavior though at slightly higher potentials being the
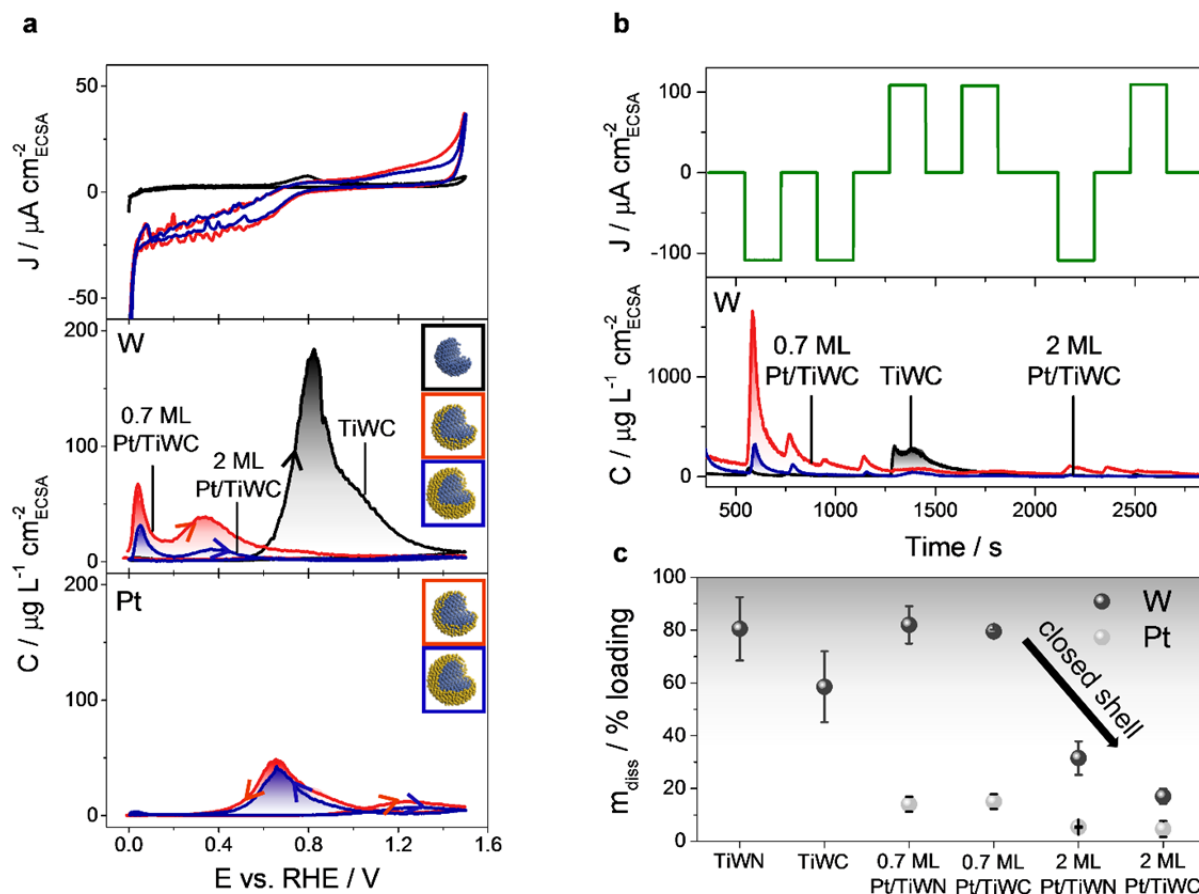99 thermodynamically more stable phase.[24,25]

Figure 1 | SFC-ICP-MS single potential cycle and galvanostatic measurements. a) First CV at 2 mV s^{-1} between 0.0 and 1.5 V$_{RHE}$ (upper panel) in 0.1 M HClO$_4$ (dilute O$_2$, see Methods) and the corresponding dissolution profiles of W (middle panel) and Pt (lower panel) as a function of potential. **b**) Applied current density profile in 0.1 M HClO$_4$ (dilute O$_2$) during the galvanostatic measurements and the corresponding dissolution profile of W with time. **c**) Total amount of metal dissolution during the galvanostatic measurements. Error bars represent standard deviation of at least 3 independent measurements.

The Pt/TiWC core-shell materials displayed a markedly different W dissolution profile compared to the bare carbide. In contrast to the single oxidative W dissolution peak for TiWC, Pt/TiWC showed two smaller dissolution peaks at lower potentials. The first peak at 0.05 V$_{RHE}$ can be attributed to the Pt-catalyzed reduction of remaining surface WO$_3$ from passivation, while the second peak at 0.35 V$_{RHE}$ corresponds to re-oxidation and subsequent dissolution of these reduced surface oxides. This effect is supported by SFC-ICP-MS experiments on Pt NPs deposited onto bulk WC, where the same two peaks were observed in the first scan from 0.0 to 0.5 V$_{RHE}$ but disappeared in later cycles (Figure S3). These peaks only reappeared after severe oxidation of WC while cycling up to 1.5 V$_{RHE}$, thus strongly indicating that the dissolution peaks below 0.5 V$_{RHE}$ are related to the initial state of the surface oxides, rather than to dissolution of WC from the bulk. From thermodynamics, the initial W dissolution occurs in the potential range corresponding to a transition from WO$_3$ to lower W oxides,[26] yet similar experiments on bulk WO$_3$ showed much less dissolution at these potentials.[24] Since these peaks appear much more noticeably in the presence of Pt, it is likely that Pt catalyzes the reduction of

123 surface WO_3, leading to the observed dissolution at low potentials. Notably, almost no
124 W dissolution was observed for the Pt/TiWC samples above 0.6 V_{RHE} where bare TiWC
125 dissolved severely. This difference is strong evidence that the Pt shell protects the
126 carbide core from dissolution at these elevated potentials, and no further W dissolution
127 was measured during the cathodic scan or the second cycle (Figure S4).

128 To obtain a more extensive overview of the stability performance, harsh galvanostatic
129 measurements were performed with the SFC-ICP-MS switching between constant
130 oxidative or reductive current densities of 0.1 mA cm^{-2}_{ECSA}. Potentials ranged
131 from -0.5 V_{RHE} under reductive currents up to 2.0 V_{RHE} under oxidative currents,
132 depending on the sample (Figure S5). The dissolution profiles for the galvanostatic
133 measurements revealed the same general features as in the single CV experiments for
134 all the samples, namely dissolution during reduction of surface oxides and during
135 oxidation of unprotected TiWC (Figure 1b). However, integration of the dissolved
136 elements over the whole galvanostatic sequence indicated that the sample with sub-ML
137 Pt coverage experienced almost complete core dissolution under these aggressive
138 conditions, while the thicker Pt shell was able to significantly suppress dissolution of the
139 carbide core (Figure 1c). The synthesis was extended to TiWN cores with 0.7 and 2 ML
140 Pt shells, which showed the same stabilizing trend with increased shell coverage
141 (Figure S5b). At potentials surpassing 1.9 V_{RHE}, much higher than the potentials at
142 which bare TiWC and TiWN NPs undergo oxidative dissolution, only 17% and 31% of W
143 dissolved for 2 ML Pt/TiWC and 2 ML Pt/TiWN, respectively. In comparison, *ca.* 80% of
144 W dissolved for both 0.7 ML Pt/TiWC and 0.7 ML Pt/TiWN, demonstrating the critical
145 importance of the Pt shell coverage and thickness for protecting the core from
146 dissolution and therefore on the overall stability of the core-shell particles. Interestingly,
147 the sub-ML Pt samples displayed even more dissolution than bare TiWC and TiWN
148 NPs, particularly for Ti (Figure S5c). We hypothesize that Pt may accelerate the
149 dissolution of exposed core surfaces at the interface through Pt-catalyzed reduction or
150 oxidation, further emphasizing the importance of complete, uniform shell coverage.

151 In addition to the dissolution behavior, we followed the structural and compositional
152 evolution of individual 2 ML Pt/TiWC NPs prior to and after an accelerated stress test
153 (AST) with IL-STEM-EDX. The AST was conducted in Ar-sat 0.1 M $HClO_4$ with 10,800
154 cycles between 0.4 and 1.0 V_{RHE} at a scan rate of 1 V s^{-1}. As shown in Figures 2 and
155 S6, particles with uniform Pt shells demonstrated remarkable stability, maintaining their
156 core-shell structure over thousands of potential cycles without leaching or forming an
157 alloy with Pt. These particles also did not agglomerate or coalesce as is typical of Pt/C
158 NPs, which is consistent with previously reported evidence for the extremely high sinter-
159 resistance of Pt/TiWC stemming from the strong bonding between the shell and the
160 core elements.[15,20] HR-STEM revealed that the carbide crystal lattice remained
161 unchanged with an interplanar distance of 0.24 nm corresponding to fcc WC(111)
162 planes (Figure 2c). Furthermore, the amounts of Pt, W, and Ti changed negligibly for
163 these particles, indicating that the atomic composition was also conserved (Figure 2d).
164 These unique findings suggest a synergistic stabilizing effect in which the Pt shell
165 protects the labile core from dissolution, while the TiWC core binds strongly to the Pt
166 shell, anchoring it in place and preventing agglomeration. Contrastingly, particles that
167 did not have complete Pt coverage showed dissolution of the TiWC core and collapsed

to form ~4-5 nm Pt NPs (Figure 2a,b). Additional IL-STEM measurements monitored the degradation of partially coated 2 ML Pt/TiWC within the first 10 cycles (Figures 2e and S7). While slight dissolution of exposed core species was observed after electrolyte contact, most dissolution and restructuring took place during the first cycle, followed by less change between cycles 1 and 10. Particles with greater core exposure dissolved more rapidly, confirming the influence of Pt coverage on the rate of core dissolution (Figure S7).
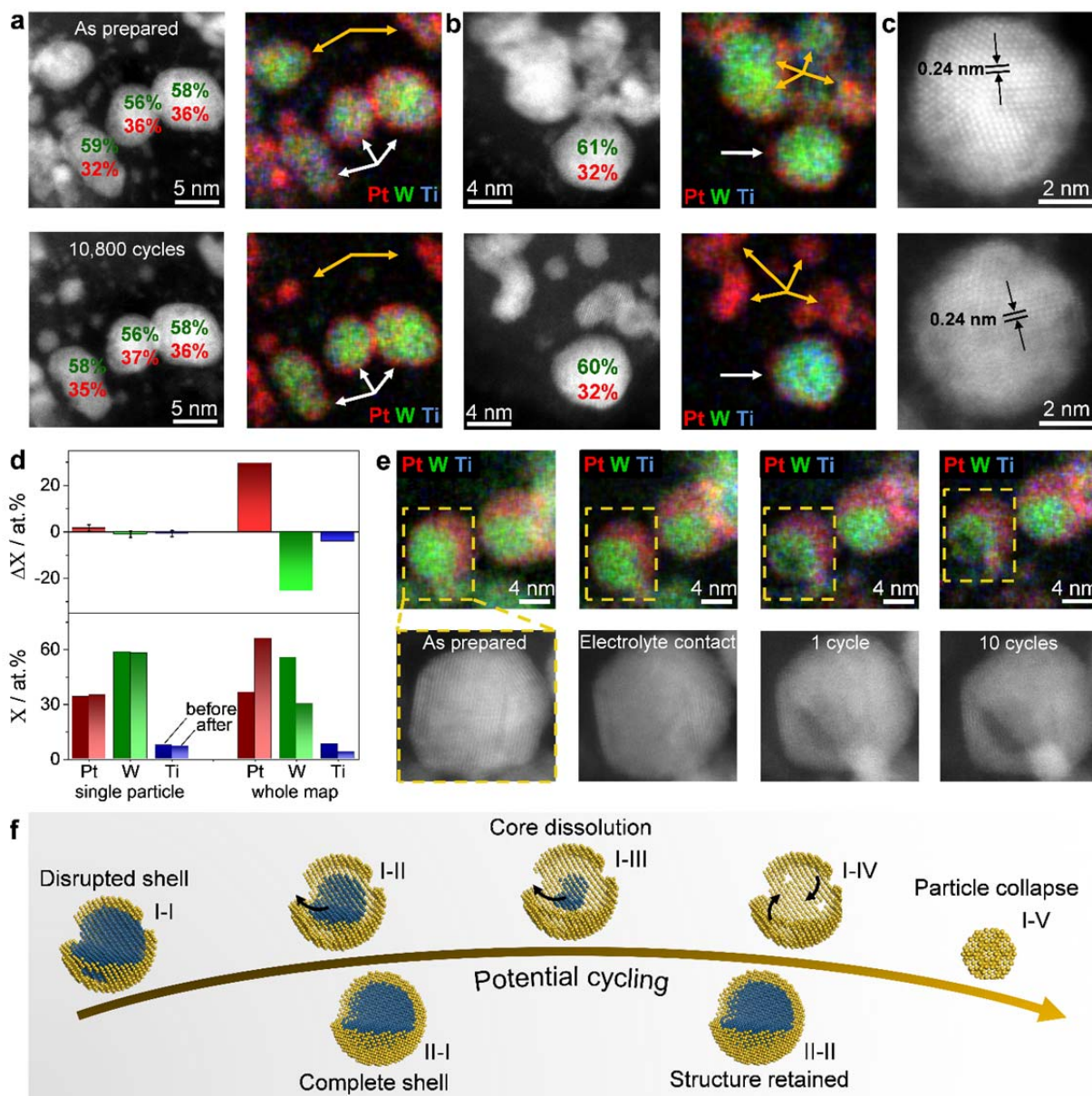

Figure 2 | Structural stability during potential cycling. a-c) Identical location STEM images and corresponding EDX elemental maps (IL-STEM-EDX) of 2 ML Pt/TiWC before (upper panel) and after (lower panel) accelerated stress tests (ASTs) showing particles with complete (white arrows) and incomplete (orange arrows) Pt shells. The AST consisted of 10,800 cycles between 0.4 and 1.0 V_{RHE} in Ar-sat 0.1 M $HClO_4$ at a scan rate of 1 V s^{-1}. **d**) Change in elemental composition measured by EDX of individual particles with complete Pt shells and the whole map after the AST. **e)** IL-STEM-EDX of 2 ML

182 Pt/TiWC as prepared, after electrolyte contact, after 1 cycle, and after 10 cycles in 0.1 M HClO$_4$. **f)**
183 Schematic showing the evolution of partially and fully coated core-shell particles during potential cycling.

185 In order to evaluate the suitability of Pt/TiWC core-shell materials for ORR applications,
186 we conducted additional long-term durability tests in O$_2$-sat electrolyte and at elevated
187 temperatures. *In situ* SFC-ICP-MS experiments measured the dissolution of 2 ML
188 Pt/TiWC over 1,000 cycles between 0.4 and 1.0 V$_{RHE}$ at 1 V s^{-1} in both Ar-sat and O$_2$-
189 sat 0.1 M HClO$_4$ at either room temperature or 60°C. Interestingly, neither the presence
190 of O$_2$ nor the increase in temperature resulted in a significant increase in dissolution.
191 For each condition, only *ca.* 3% of W and 0.1% of Pt dissolved in total during the 1,000
192 cycles (Figure S8b), the majority of which occurred during the first 400 cycles, likely due
193 to the presence of core-shell particles with incomplete Pt coverage (Figure 3a).
194 Following this initial period, minimal dissolution occurred with 0.1% or less of W and
195 undetectable amounts of Pt dissolving in total over the last 100 cycles. These results
196 suggest that homogeneously coated 2 ML Pt/TiWC particles are completely stable in
197 O$_2$-sat electrolyte at elevated temperatures. This was further confirmed by STEM-EDX,
198 which showed preservation of the core-shell structure after the AST consisting of 10,800
199 cycles between 0.4 and 1.0 V$_{RHE}$ in O$_2$-sat 0.1 M HClO$_4$ at 60°C (Figure 3b).
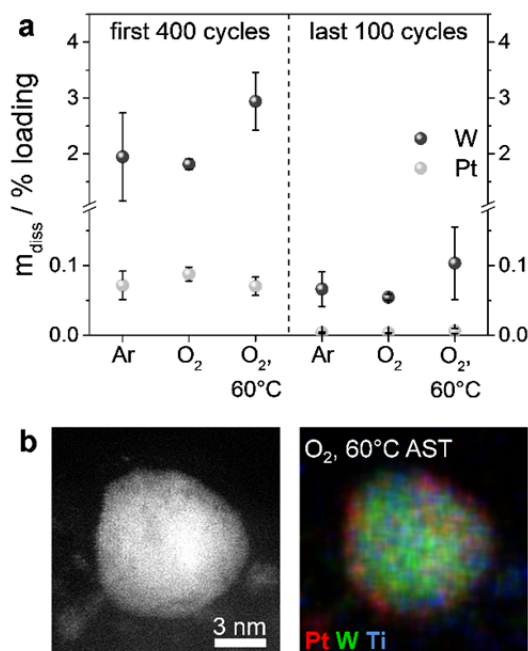

201

202 **Figure 3 | Long-term durability in O$_2$-sat electrolyte and at elevated temperature. a)** Total amount of
203 W and Pt dissolution measured via SFC-ICP-MS for 2 ML Pt/TiWC during the first 400 and last 100 cycles
204 of an AST consisting of 1,000 cycles from 0.4 to 1.0 V$_{RHE}$ at 1 V s^{-1} in Ar or O$_2$-sat 0.1 M HClO$_4$ at room
205 temperature or 60°C. Error bars represent standard deviation of at least 3 independent measurements. **b)**
206 STEM image and corresponding EDX elemental map of a 2 ML Pt/TiWC NP after 10,800 cycles from 0.4
207 to 1.0 V$_{RHE}$ at 1 V s^{-1} in O$_2$-sat 0.1 M HClO$_4$ at 60°C.

208 The durability of 2 ML Pt/TiWC as an ORR catalyst was further evaluated by comparing
209 its activity and electrochemical surface area (ECSA) before and after 10,800 cycles in

210   O$_2$-sat electrolyte to those of a commercial Pt/C catalyst (TKK, 46 wt.%, 3 nm) (Figure
211   4). The ORR activity was obtained via thin film rotating disk electrode (RDE)
212   measurements at 1,600 rpm in O$_2$-sat 0.1 M HClO$_4$, and the Pt ECSA was measured
213   from CO stripping (Figures S11 and S12). Initially, 2 ML Pt/TiWC displayed an
214   enhanced specific activity of 0.69 mA cm$^{-2}_{Pt}$ over Pt/C (0.47 mA cm$^{-2}_{Pt}$), which may be
215   attributed to a weaker oxygen binding energy[27] resulting from its slightly downshifted Pt
216   d-band center relative to pure Pt.[28] After the AST with O$_2$, the Pt/C control showed a
217   19% loss in ECSA, 36% loss in mass activity, and 22% loss in specific activity, similar to
218   previous work by Hasché et al.[29] In contrast, 2 ML Pt/TiWC showed only a 9% loss in
219   ECSA, 22% loss in mass activity, and 14% loss in specific activity. For Pt/C, multiple
220   mechanisms have been reported to contribute to the significant decrease in ECSA after
221   cycling, including agglomeration, Ostwald ripening, dissolution, and particle
222   detachment.[13,30] For 2 ML Pt/TiWC, the losses in performance can all be linked to the
223   corrosion of imperfect core-shell particles, as other degradation mechanisms were not
224   observed in the IL-STEM-EDX or *in situ* SFC-ICP-MS experiments. When these
225   imperfect particles restructured and collapsed, the ECSA decreased slightly from the
226   loss of Pt surface sites into the bulk of the newly formed Pt NPs, while the specific
227   activity dropped more substantially due to the lower activity of Pt NPs compared to 2 ML
228   Pt/TiWC. Thus, further optimization of the synthesis method to produce more uniform
229   core-shell particles should result in even greater improvement in performance.
230   Evidently, these results demonstrate the enhanced catalytic stability of the core-shell
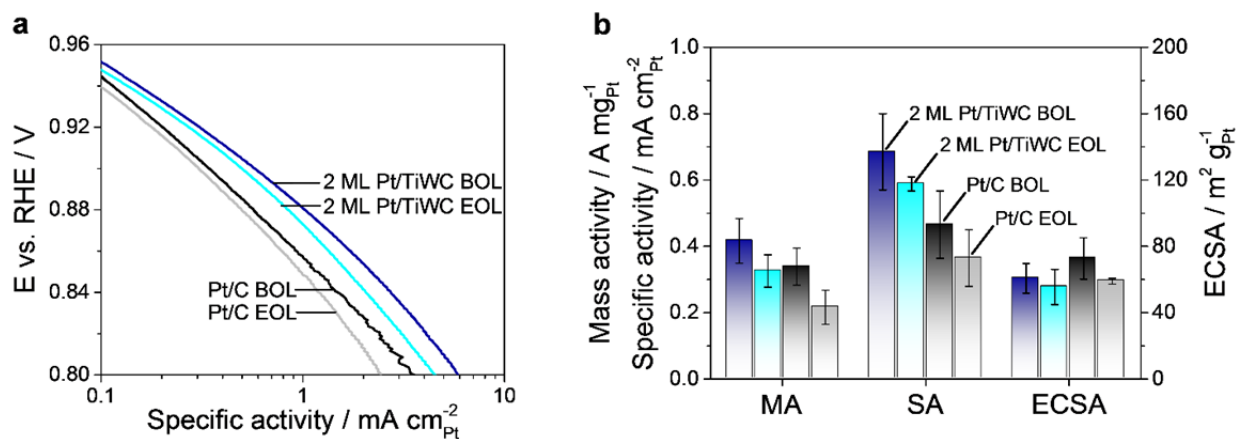231   material over traditional monometallic Pt/C catalysts.

233   **Figure 4 | ORR catalytic stability. a**) Tafel plots normalized to electrochemical surface area (ECSA)
234   before (BOL) and after (EOL) accelerated stress tests (ASTs) consisting of 10,800 cycles between 0.4
235   and 1.0 V$_{RHE}$ in O$_2$-sat 0.1 M HClO$_4$ at a scan rate of 1 V s^{-1}. **b**) Mass activity (MA) at 0.9 V$_{RHE}$, specific
236   activity (SA) at 0.9 V$_{RHE}$, and ECSA from CO stripping before and after ASTs in O$_2$-sat 0.1 M HClO$_4$.
237   Activity was determined from background and iR-corrected ORR polarization curves in O$_2$-sat 0.1 M
238   HClO$_4$ at 50 mV s^{-1} and 1,600 rpm with Pt loading of 5 µg$_{Pt}$ cm^{-2} for 2 ML Pt/TiWC and 20 µg$_{Pt}$ cm^{-2} for
239   Pt/C (TKK, 46 wt.%). Error bars represent standard deviation of at least 3 independent measurements.

240   In summary, we have shown how nanostructured core-shell materials with TMC or TMN
241   cores can be engineered to have high stability in harsh, oxidative electrochemical
242   environments. SFC-ICP-MS and IL-STEM-EDX experiments revealed the ability of
243   atomically-thin Pt shells to protect the TiWC and TiWN cores against dissolution while

emphasizing the need for complete, uniform shell coverage. Notably, 2 ML Pt/TiWC NPs with a homogeneous Pt coating exhibited no degradation in the core-shell structure or atomic composition during ASTs with over 10,000 potential cycles in O_2-sat electrolyte at elevated temperatures. This unique performance, including the absence of leaching, alloying, and agglomeration, arises specifically from the stabilizing interaction between the noble metal shell and the TMC core. In addition, the increased catalytic durability compared to Pt/C for ORR highlights potential industrial applications. These results provide detailed insight into the underlying degradation mechanisms that affect the stability of core-shell nanomaterials and also illustrate promising design strategies utilizing earth-abundant TMC and TMN cores to develop low-cost, ultradurable core-shell catalysts.

References

1. Strasser, P. et al. Lattice-strain control of the activity in dealloyed core-shell fuel cell catalysts. *Nat. Chem.* **2**, 454-460 (2010).
2. Gasteiger, H. A. & Marković, N. M. Just a Dream—or Future Reality? *Science* **324**, 48-49 (2009).
3. Stephens, I. E. L., Bondarenko, A. S., Grønbjerg, U., Rossmeisl, J. & Chorkendorff, I. Understanding the electrocatalysis of oxygen reduction on platinum and its alloys. *Energy Environ. Sci.* **5**, 6744-6762 (2012).
4. Oezaslan, M., Hasché, F. & Strasser, P. Pt-Based Core–Shell Catalyst Architectures for Oxygen Fuel Cell Electrodes. *J. Phys. Chem. Lett.* **4**, 3273-3291 (2013).
5. Wang, X. et al. Palladium-platinum core-shell icosahedra with substantially enhanced activity and durability towards oxygen reduction. *Nat. Commun.* **6**, 7594 (2015).
6. Schwammlein, J. N. et al. Origin of Superior Activity of Ru@Pt Core-Shell Nanoparticles towards Hydrogen Oxidation in Alkaline Media. *ECS Trans.* **75**, 971-982 (2016).
7. Alayoglu, S., Nilekar, A. U., Mavrikakis, M. & Eichhorn, B. Ru-Pt core-shell nanoparticles for preferential oxidation of carbon monoxide in hydrogen. *Nat. Mater.* **7**, 333-338 (2008).
8. Sasaki, K. et al. Core-Protected Platinum Monolayer Shell High-Stability Electrocatalysts for Fuel-Cell Cathodes. *Angew. Chem. Int. Ed.* **49**, 8602-8607 (2010).
9. Tedsree, K. et al. Hydrogen production from formic acid decomposition at room temperature using a Ag-Pd core-shell nanocatalyst. *Nat. Nanotech.* **6**, 302-307 (2011).
10. Strickler, A. L., Jackson, A. & Jaramillo, T. F. Active and Stable Ir@Pt Core–Shell Catalysts for Electrochemical Oxygen Reduction. *ACS Energy Lett.* **2**, 244-249 (2016).
11. Cui, C., Gan, L., Heggen, M., Rudi, S. & Strasser, P. Compositional segregation in shaped Pt alloy nanoparticles and their structural behaviour during electrocatalysis. *Nat. Mater.* **12**, 765-771 (2013).
12. Chen, S., Gasteiger, H. A., Hayakawa, K., Tada, T. & Shao-Horn, Y. Platinum-Alloy Cathode Catalyst Degradation in Proton Exchange Membrane Fuel Cells: Nanometer-Scale Compositional and Morphological Changes. *J. Electrochem. Soc.* **157**, A82-A97 (2010).
13. Perez-Alonso, F. J. et al. Identical locations transmission electron microscopy study of Pt/C electrocatalyst degradation during oxygen reduction reaction. *J. Power Sources* **196**, 6085-6091 (2011).
14. Knossalla, J. *et al.* Shape-Controlled Nanoparticles in Pore-Confined Space. *J. Am. Chem. Soc.* **140**, 15684-15689, (2018).
15. Hunt, S. T. et al. Self-assembly of noble metal monolayers on transition metal carbide nanoparticle catalysts. *Science* **352**, 974-978 (2016).
16. Zhong, Y. et al. Transition Metal Carbides and Nitrides in Energy Storage and Conversion. *Adv. Sci.* **3**, 1500286 (2016).
17. Hunt, S. T., Nimmanwudipong, T. & Roman-Leshkov, Y. Engineering non-sintered, metal-terminated tungsten carbide nanoparticles for catalysis. *Angew. Chem.* **53**, 5131-5136 (2014).
18. Kuttiyiel, K. A. et al. Enhancement of the oxygen reduction on nitride stabilized pt-M (M=Fe, Co, and Ni) core–shell nanoparticle electrocatalysts. *Nano Energy* **13**, 442-449 (2015).

295 19. Tian, X. et al. Transition Metal Nitride Coated with Atomic Layers of Pt as a Low-Cost, Highly Stable
296   Electrocatalyst for the Oxygen Reduction Reaction. *J. Amer. Chem. Soc.* **138**, 1575-1583 (2016).
297 20. Garg, A. et al. Transition-Metal Nitride Core@Noble-Metal Shell Nanoparticles as Highly CO Tolerant
298   Catalysts. *Angew. Chem. Int. Ed.* **56**, 8828-8833 (2017).
299 21. Hunt, S. T., Milina, M., Wang, Z. & Roman-Leshkov, Y. Activating earth-abundant electrocatalysts for
300   efficient, low-cost hydrogen evolution/oxidation: sub-monolayer platinum coatings on titanium
301   tungsten carbide nanoparticles. *Energy Environ. Sci.* **9**, 3290-3301 (2016).
302 22. Garg, A. Transition Metal Carbide and Nitride Nanoparticles with Noble Metal Shells as Enhanced
303   Catalysts. (Massachusetts Institute of Technology, 2018).
304 23. Topalov, A. A. et al. Dissolution of platinum: limits for the deployment of electrochemical energy
305   conversion? *Angew. Chem.* **51**, 12613-12615 (2012).
306 24. Göhl, D. et al. Electrochemical stability of hexagonal tungsten carbide in the potential window of fuel
307   cells and water electrolyzers investigated in a half-cell configuration. *Electrochim. Acta* **270**, 70-76
308   (2018).
309 25. Weidman, M. C., Esposito, D. V., Hsu, I. J. & Chen, J. G. Electrochemical Stability of Tungsten and
310   Tungsten Monocarbide (WC) Over Wide pH and Potential Ranges. *J. Electrochem. Soc.* **157**, F179-
311   F188 (2010).
312 26. Pourbaix, M. *Atlas of Electrochemical Equilibria in Aqueous Solutions* (National Association of
313   Corrosion Engineers, Houston, 1974).
314 27. Greeley, J. et al. Alloys of platinum and early transition metals as oxygen reduction electrocatalysts.
315   *Nat. Chem.* **1**, 552-556 (2009).
316 28. Hendon, C. H. et al. Realistic Surface Descriptions of Heterometallic Interfaces: The Case of TiWC
317   Coated in Noble Metals. *J. Phys. Chem. Lett.* **7**, 4475-4482 (2016).
318 29. Hasche, F., Oezaslan, M. & Strasser, P. Activity, stability and degradation of multi walled carbon
319   nanotube (MWCNT) supported Pt fuel cell electrocatalysts. *Phys. Chem. Chem. Phys.* **12**, 15251-
320   15258 (2010).
321 30. Meier, J. C. et al. Design criteria for stable Pt/C fuel cell catalysts. *Beilstein J. Nanotechnol.* **5**, 44-67
322   (2014).

Acknowledgements

Author Contributions

D.G., A.G., Y.R.-L., and M.L. conceived this study. A.G. synthesized the materials and performed physicochemical characterization. D.G. conducted the electrochemical stability measurements via SFC-ICP-MS. P.P. carried out IL-STEM measurements accompanied with EDX elemental mapping. D.G. and A.G. conducted ORR activity measurements via RDE. The manuscript was written by A.G., Y.R.-L., D.G., and M.L. All authors discussed the manuscript and the results.

Competing Interests

The authors declare no competing interests.

Methods

Materials synthesis. Silica encapsulated titanium tungsten oxide NPs coated with a desired amount of Pt salt (denoted as $SiO_2/(NH_4)_2PtCl_6/TiWO$) were synthesized using a reverse microemulsion (RME) method by first mixing n-heptane, Brij-L4® surfactant, ultrapure water (18 MΩ·cm), NH_4OH solution, tungsten isopropoxide, and titanium isopropoxide. The mixture was stirred for 4 h to allow the $Ti_{0.1}W_{0.9}O_x$ NPs to form. Afterward, a separate RME containing n-heptane, Brij-L4®, and chloroplatinic acid dissolved in water was added dropwise to the first RME causing the precipitation of the Pt salt onto the TiWO NPs. After another 4 h, tetraethyl orthosilicate was added and left to react for 16.5 h, encapsulating the particles in a SiO_2 shell. Then, methanol was added to precipitate the $SiO_2/(NH_4)_2PtCl_6/TiWO$ NPs, which were recovered after centrifugation and washing with acetone. $SiO_2/Pt/TiWC$ core-shell particles were formed by heating the oxide powder up to 900°C at a ramp rate of 2°C min^{-1} under a gas flow of 15% CH_4-85% H_2 and held for 5 h. After cooling to room temperature under H_2, the samples were passivated using 1% O_2-99% N_2 flow. The SiO_2 was removed by dissolution in a mixture of degassed ethanol and aqueous HF solution for 18 h at room temperature with dispersed carbon black added as a support. The carbon-supported Pt/TiWC NPs were recovered through centrifugation, washed thoroughly with degassed ethanol and water, and dried under vacuum. To synthesize Pt/TiWN, the Pt/TiWC powder was heated up to 800°C at a ramp rate of 2°C min^{-1} under NH_3 flow and held for 3 h. After cooling to room temperature under NH_3, the samples were passivated. Complete synthetic details are provided in ref. [20].

Pt NPs were synthesized via the ethylene glycol (EG) route described in literature. Here, 3.13 mL of a H_2PtCl_6 solution in water (8 wt.%, Sigma-Aldrich) were dissolved in 22 mL of EG and mixed with 25 mL of a 0.5 M NaOH solution in EG. The mixture was heated up to 150°C while stirring and held there for 1.5 h after its color turned from orange to brownish black. After the completion of the reaction, 3 mL of a 1 M HCl solution were added to precipitate the NPs, which were recovered through centrifugation and washing with 1 M HCl. Once dried, the Pt NPs were dispersed in acetone along with WC particles (d=190 nm, Sigma-Aldrich) via ultrasonication while evaporating the solvent. The deposition on WC was confirmed via TEM imaging on a JEOL JEM 2200FS operating at 200 kV. For the SFC measurements, Pt NPs/bulk WC was re-dispersed in water and deposited on a GC plate with a total loading of 1 and 0.25 µg of W and Pt, respectively. The dissolution was measured during a potential cycle sequence at 2 mV s^{-1} consisting of 2 cycles up to 0.5 V_{RHE} followed by 1 cycle up to 1.5 V_{RHE} and ending with 1 more cycle up to 0.5 V_{RHE}.

Characterization. Powder X-ray diffraction (PXRD) was performed on a Bruker D8 diffractometer using Cu Kα radiation with a step size of 0.02° and step time of 0.2 s. TEM was performed on a JEOL 2010F equipped with a field emission gun operating at 200 kV. Sample elemental composition was measured on an Agilent 7900 ICP-MS. IL-STEM was performed on a FEI Titan 80-200 (ChemiSTEM) with a C_s-corrector (CEOS GmbH) and a high angle annular dark field (HAADF) detector. The microscope was operated at 80 kV to minimize beam damage. "Z-contrast" conditions were achieved using a probe semi-convergence angle of 24.7 mrad and an inner collection semi-angle of 88.4 mrad. Elemental maps were recorded by EDX using four large solid angle symmetrical Si drift detectors. For the quantification, Pt L, W L, and Ti K-edges were used.

SFC-ICP-MS measurements. 0.7 µL of aqueous catalyst suspension was drop-casted onto a polished glassy carbon (GC) plate and enclosed by the opening of the SFC. The loading for Pt and W on the GC plate was 0.03 and 0.15 µg/spot, respectively. An Ag/AgCl reference electrode was placed behind the outlet of the SFC and was calibrated against a RHE prior to each measurement. A graphite rod counter electrode was placed before the inlet. The 0.1 M $HClO_4$ electrolyte was stored in a small reservoir where it was purged with Ar or O_2 and then pumped at a constant flow rate of 380 µL min^{-1} through the SFC and into the ICP-MS (Perkin Elmer NexION 350X). Although the electrolyte was initially purged with Ar, slight O_2 intrusion could not be avoided resulting in a dilute O_2 concentration about 100 times less than the saturation limit. After the electrolyte left the SFC, it was mixed via a V-connector with an internal standard containing 10 µg L^{-1} Re and Sc and then introduced into the ICP-MS. The Sc^{45}, Ti^{47}, W^{184}, Re^{187}, and Pt^{195} isotopes were used to measure the concentration in the electrolyte. The delay time of 17 s between dissolution at the working electrode and detection at the ICP-MS was compensated by calibrating the time scale. The current density and the concentration of dissolved metals were normalized to the ECSA. For samples containing Pt, the value obtained from CO stripping during RDE tests was used. For samples

397   without Pt, the ECSA was estimated assuming an average particle size of 5 nm. Complete details on the
398   SFC-ICP-MS setup are provided in ref. [31].

399   For the single potential cycle experiments, samples were pretreated with 0.5 M NaOH and rinsed
400   with ultrapure water in order to reduce the amount of surface oxides and improve the resolution of the
401   experiment. Then, a slow CV scan at 2 mV s^{-1} from 0.0 to 1.5 V_{RHE} was conducted. All potentials are
402   reported versus the reversible hydrogen electrode (RHE). For the galvanostatic experiments, there was
403   no NaOH pretreatment to allow for quantitative comparison of the overall amount of dissolved metal.
404   These experiments began with 2 reductive cycles, followed by 2 oxidative, 1 reductive, and finally 1
405   oxidative cycle. Each cycle consisted of a 3 min period at open circuit voltage (OCV) followed by a 3 min
406   period at a current density of ±0.1 mA cm$^{-2}_{ECSA}$ according to whether it was a reductive or oxidative cycle.
407   For the long-term durability experiments, the dissolution was measured during an AST consisting of 1,000
408   cycles from 0.4 to 1.0 V_{RHE} at 1 V s^{-1} in Ar or O_2-sat 0.1 M $HClO_4$ at room temperature or 60°C.

410   **IL-STEM measurements.** 10 µL of an aqueous catalyst suspension (0.05 g_{cat} L^{-1}) was drop-casted on a
411   gold TEM finder grid (S147A9, Plano GmbH) and dried. After acquiring several HAADF STEM images of
412   different regions and the corresponding elemental maps, the catalyst-coated TEM grid was used as a
413   working electrode for the AST consisting of 10,800 cycles between 0.4 and 1.0 V_{RHE} at 1 V s^{-1} in Ar-sat or
414   O_2-sat 0.1 M $HClO_4$ at room temperature or 60°C. A Gaskatel HydroFlex RHE was used as the reference
415   electrode and a graphite rod as the counter electrode. The potential was controlled by a Bio-Logic
416   Science Instruments SP-50 potentiostat. The iR drop was measured by the current interrupt method and
417   corrected for. After the AST, the grid was rinsed with ultrapure water to remove electrolyte residues and
418   dried. The grid was then re-analyzed at identical locations.

420   **RDE measurements.** The measurements were performed at room temperature on a Gamry Reference
421   600 potentiostat with an in-house developed RDE setup. Prior to measurements, the iR drop in the cell
422   was determined by high frequency impedance. A three-compartment Teflon cell was used with a graphite
423   rod counter electrode and Ag/AgCl reference electrode separated by a Nafion® membrane (Tschurl
424   modification) to avoid chloride contamination. The reference electrode was calibrated against a reversible
425   hydrogen electrode (RHE) prior to each measurement and all potentials are reported versus RHE.
426   Catalyst suspensions were prepared by sonicating the samples in 1 mL ultrapure water (Elga PURELAB®
427   Plus, 18 MΩ·cm, TOC < 3 ppb) for 30 min with the concentration of Pt and W as 0.05 and 0.1 g L^{-1},
428   respectively. 20 µL of this suspension was loaded onto a polished 5 mm GC RDE tip and then dried to
429   form the working electrode. The Pt loading was 5 µg$_{Pt}$ cm$^{-2}_{geo}$ for 2 ML Pt/TiWC and 20 µg$_{Pt}$ cm$^{-2}_{geo}$ for
430   Pt/C (TKK, 46 wt.%). The 0.1 M $HClO_4$ electrolyte was prepared from ultrapure water and 70% $HClO_4$
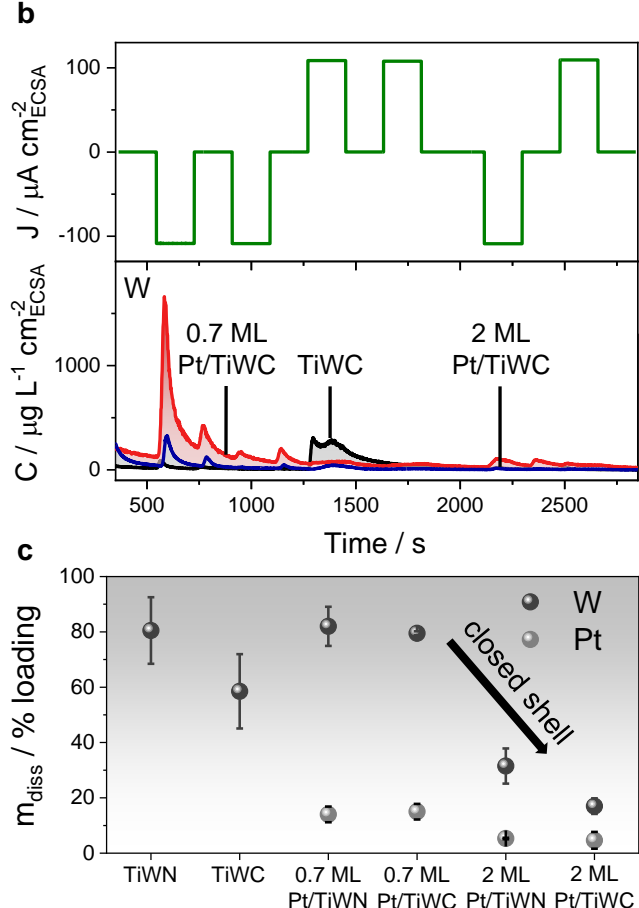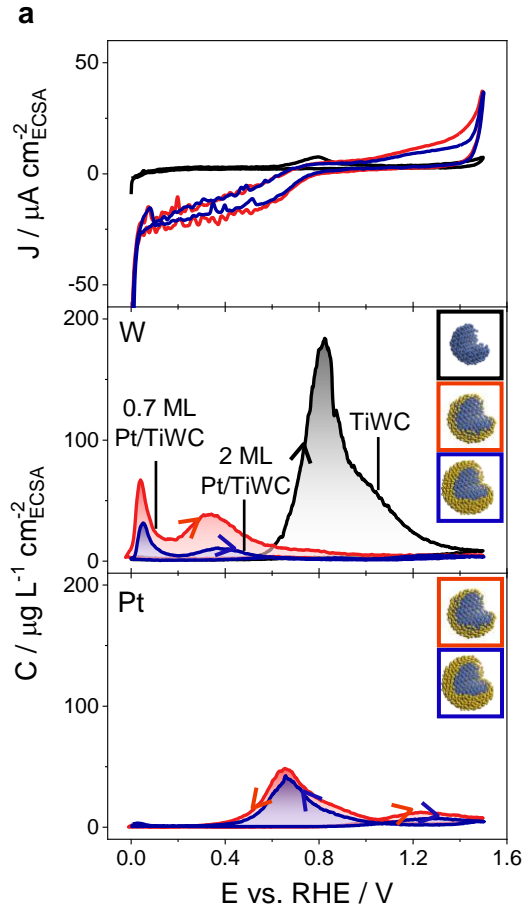431   (Merck Suprapur®).

432   The catalyst surface was first pretreated in Ar-sat electrolyte with 20 cyclic voltammetry (CV)
433   conditioning scans from 0.05 to 1.0 V_{RHE} at 200 mV s^{-1}. Afterwards, ORR polarization curves were
434   recorded in O_2-sat electrolyte at 50 mV s^{-1} and 1,600 rpm with iR compensation. A background was
435   recorded in Ar-sat electrolyte using identical conditions and subtracted to obtain the ORR current. CO
436   stripping and hydrogen underpotential deposition (H$_{upd}$) measurements were performed to calculate
437   ECSA values using a conversion factor of 390 and 195 µC cm$^{-2}_{Pt}$, respectively, according to ref. [32]. A CV
438   at 50 mV s^{-1} and 0 rpm was recorded to calculate the H$_{upd}$ ECSA, which was done after subtracting the
439   background in CO-sat electrolyte. To obtain the CO stripping voltammograms, the electrode was held at
440   0.05 V_{RHE} as the electrolyte was purged with CO for 7 min to saturate the surface and then with Ar for 25
441   min to remove excess CO. Immediately after, a CV was recorded from 0.05 to 1.0 V_{RHE} at 50 mV s^{-1}. CO
442   stripping did not lead to enhanced degradation or restructuring (Figure S9), and the values obtained by
443   the two methods were very similar (Figure S11). The catalytic stability was evaluated using an AST
444   protocol consisting of 10,800 cycles between 0.4 and 1.0 V_{RHE} at 1 V s^{-1} in O_2-sat 0.1 M $HClO_4$ at room
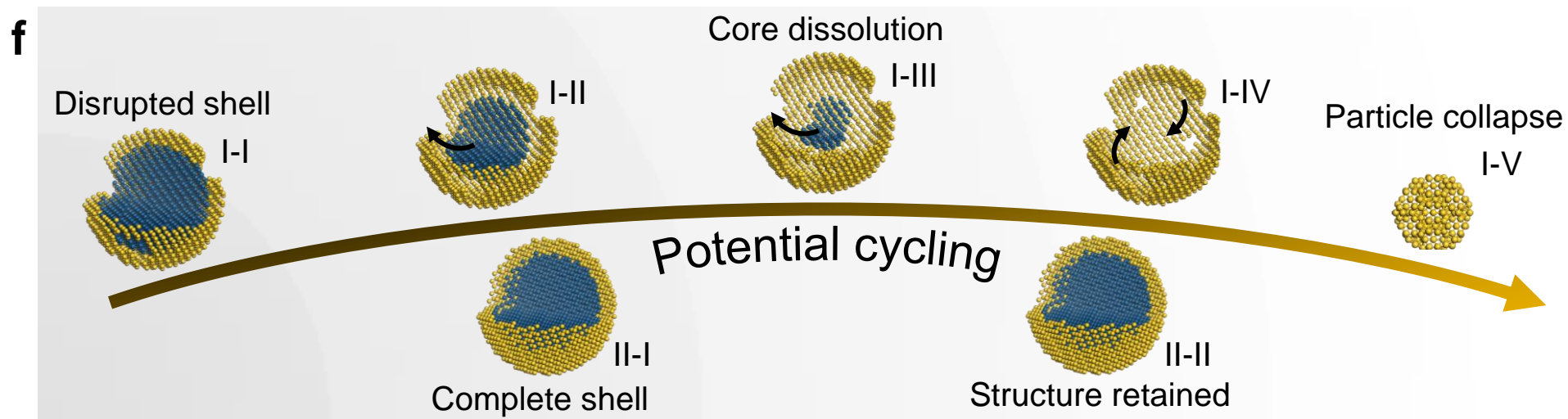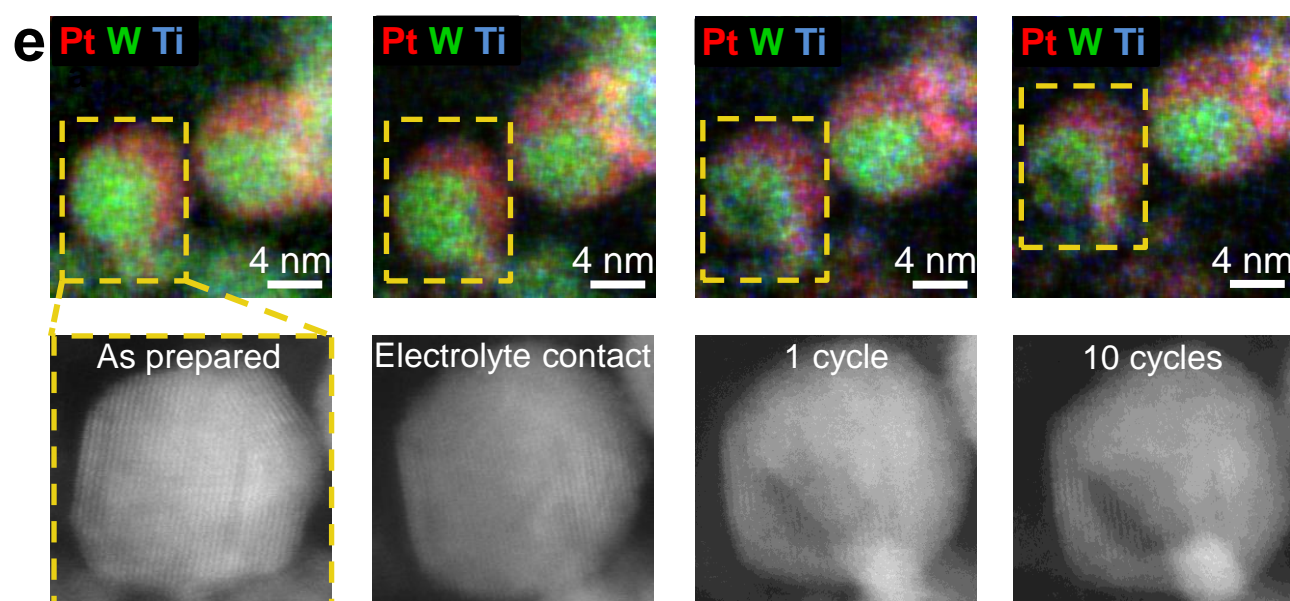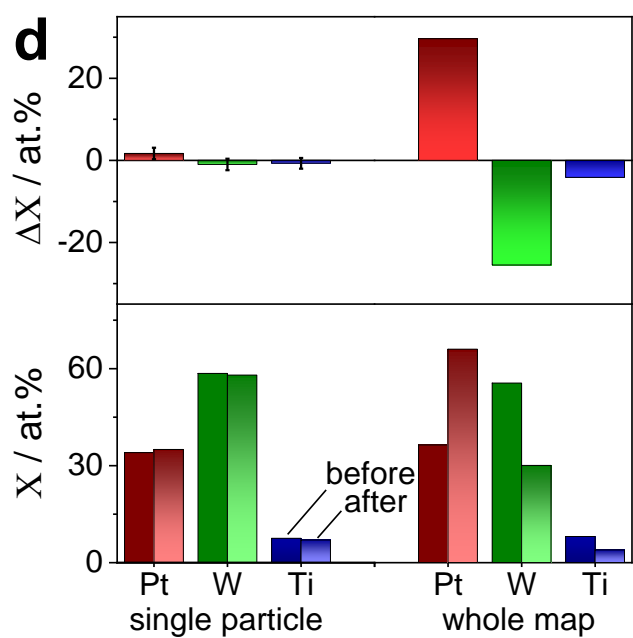445   temperature.

447   **Data availability**
448   Experimental data are available from the corresponding authors on reasonable request.

450   **References**

451 31. Grote, J.-P., Zeradjanin, A. R., Cherevko, S. & Mayrhofer, K. J. J. Coupling of a scanning flow cell
452   with online electrochemical mass spectrometry for screening of reaction selectivity. *Rev. Sci. Instrum.*
453   **85**, 104101 (2014).
454
455 32. Mayrhofer, K. J. J. et al. Measurement of oxygen reduction activities via the rotating disc electrode
456   method: From Pt model surfaces to carbon-supported high surface area catalysts. *Electrochim. Acta*
457   **53**, 3181-3188 (2008).
458
459

a
As prepared
56% 58%
36% 36%
59%
32%
5 nm
Pt W Ti

10,800 cycles
56% 58%
37% 36%
58%
35%
5 nm
Pt W Ti

b
61%
32%
4 nm
Pt W Ti

60%
32%
4 nm
Pt W Ti

c
0.24 nm
2 nm

0.24 nm
2 nm

d
ΔX / at.%
X / at.%
before
after
Pt W Ti
single particle
Pt W Ti
whole map

e
Pt W Ti   Pt W Ti   Pt W Ti   Pt W Ti
4 nm   4 nm   4 nm   4 nm
As prepared   Electrolyte contact   1 cycle   10 cycles

f
Core dissolution
Disrupted shell
I-I   I-II   I-III   I-IV
Particle collapse
I-V
Potential cycling
II-I
Complete shell
II-II
Structure retained

a

first 400 cycles | last 100 cycles

W
Pt

m_{diss} / % loading

Ar   O$_2$ O$_2$, 60°C   Ar   O$_2$ O$_2$, 60°C

b

O$_2$, 60°C AST

3 nm

Pt W Ti

a

E vs. RHE / V

Specific activity / mA cm$_{Pt}^{-2}$

2 ML Pt/TiWC BOL
2 ML Pt/TiWC EOL
Pt/C BOL
Pt/C EOL

b

Mass activity / A mg$_{Pt}^{-1}$
Specific activity / mA cm$_{Pt}^{-2}$
ECSA / m^2 g$_{Pt}^{-1}$

2 ML Pt/TiWC BOL
2 ML Pt/TiWC EOL
Pt/C BOL
Pt/C EOL

MA   SA   ECSA